Development of a Compact MRI System for Trabecular Bone Microstructure Measurements of the Distal Radius

Shinya Handa,[1]* Sadanori Tomiha,[1] Tomoyuki Haishi,[2] and Katsumi Kose[1]

A compact MRI system for trabecular bone (TB) microstructure measurements of the distal radius was developed using a 1.0 T permanent magnet and a compact MRI console. TB microstructure of the distal radius was clearly visualized using a three-dimensional (3D) driven equilibrium spin-echo (DESE) sequence in 23 min. The image obtained had a sufficient spatial resolution (150 μm × 150 μm × 500 μm) and signal-to-noise ratio (SNR) (approximately 10) for 3D bone microstructure analysis. The system demonstrated the feasibility of using a permanent magnet compact MRI system as a clinical instrument for bone microstructure measurements of the distal radius. Magn Reson Med 58:225–229, 2007. © 2007 Wiley-Liss, Inc.

Key words: dedicated MRI; distal radius; trabecular bone; bone microstructure; driven equilibrium spin-echo.

Measurements of trabecular bone (TB) microstructure are essential for assessment of bone fracture risk and evaluation of drug therapy in osteoporosis (1–6). TB microstructure has been measured using extremity RF coils and sophisticated imaging pulse sequences in whole-body MRI systems (7–12). Recently, a compact MRI for the human finger (13) and high-resolution X-ray CT systems for human extremities have been reported as new instruments for TB microstructure measurements (14).

Because X-ray CT systems use ionizing radiation, high-resolution MRI systems have a definite advantage in terms of patient safety. Although the finger MRI system has advantages of spatial resolution and compactness, the finger is not a well-accepted site for bone microstructure evaluation. Therefore, if we can construct a compact MRI to measure a well-accepted site, such as the distal radius, tibia, and calcaneus, for TB microstructure analysis, the system will be a useful instrument for diagnosis of osteoporosis.

In this work we have developed a compact MRI for measurements of the distal radius using a 1.0 T permanent magnet and a compact MRI console. Using this system, we have successfully obtained high-resolution images of the distal radius that could be used for TB microstructure analysis.

MATERIALS AND METHODS

Compact MRI System for the Distal Radius

Figure 1a shows an overview of the compact MRI system developed in this study. The system consists of a permanent magnet (NEOMAX, Osaka, Japan), gradient coil set, RF probe, and compact MRI console (15–17). The entire system can be installed in a 1 m × 2 m space.

The permanent magnet is U-shaped using Nd-B-Fe material (18,19). Its specifications are: field strength = 1.02 T, gap width = 100 mm, homogeneity = 16.4 ppm over 60 mm diameter spherical volume, size = 539 mm (width) × 706 mm (height) × 1029 mm (depth), and total weight = 1340 kg. Because the magnet was designed for in vivo imaging of rats and mice, its shape was not optimized for in vivo imaging of human extremities. The magnet temperature was regulated at around 30°C to minimize temperature drift of the Larmor frequency using a magnet heating system with a proportional-integral-derivative (PID) temperature controller. The typical frequency drift during the image acquisition was about 110 Hz/min, which was corrected using the NMR lock technique described later.

Because the magnet gap space was very limited, a flat and circular gradient coil set (diameter = 200 mm, thickness = 5.0 mm) with a conventional design (axial coil: Maxwell pair; transverse coil: parallel four wires) was developed. The gradient coil set comprised flat coil elements made of polyethylene coated copper wires (diameter = 0.8 mm). The coil elements were piled up on 2.0 mm thick Bakelite plates and fixed on the pole pieces of the magnet. The efficiencies of the gradient coils were 0.66, 0.70, 0.98 G/cm/A for G_x, G_y, and G_z, respectively.

An RF probe box made of brass and copper plates was developed for imaging of the distal radius (Fig. 1b). A six-turn solenoid coil with an oval aperture (55 mm width and 75 mm height) and 40 mm length was made of a Cu tape (width = 5 mm and thickness = 0.1 mm). The RF coil was split with 11 chip capacitors (100 pF) to obtain a sharp resonance at 43.4 MHz. Unloaded and loaded Q factors of the RF coil at 43.4 MHz were 232 and 98, respectively. The RF coil was used both for transmit and receive.

The configuration of the permanent magnet, gradient coil set, and RF probe were shown in Fig. 2.

The MRI console consisted of an industrial personal computer, MRI transceiver (DTRX4; MRTechnology, Tsukuba, Japan), three-channel gradient driver (±50 V, ±20 A; Jyonan Electric Laboratory, Tsukuba, Japan), and class AB narrowband RF power amplifier (43 MHz, 200 W; TOKYO HY-POWER LABS, Tokyo, Japan).

The MRI signal receiving system was developed using the MRI transceiver, a variable gain amplifier (VGA), and a narrow bandwidth preamplifier (noise figure (NF) = 1.0 dB, gain = 50 dB). The VGA has a wide amplification range (−30 dB to 30 dB) controlled by an external reference direct current (DC) voltage. To extend the dynamic range of the MRI receiving system, the gain of the VGA was dynamically changed in the imaging pulse sequence ac-

[1]Institute of Applied Physics, University of Tsukuba, Tsukuba, Japan.
[2]MRTechnology, Inc., Tsukuba, Japan.
*Correspondence to: Shinya Handa, Institute of Applied Physics, University of Tsukuba, Tsukuba 305-8573, Japan. E-mail: handa@mrlab.frsc.tsukuba.ac.jp
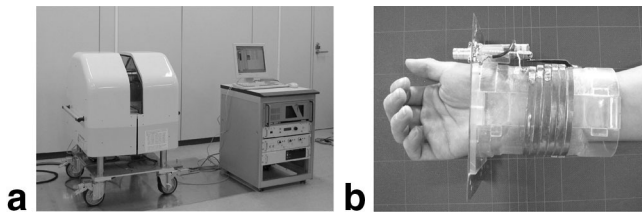
FIG. 1. The compact MRI system for trabecular bone measurements of the distal radius. **a:** System overview. **b:** Open view of the RF coil.

cording to the spatial frequency in *k*-space. As a result, the receiving system achieved the dynamic range of about 90 dB, sufficient for acquisition of 3D spin-echo (SE) images of the distal radius.

Phantom and Subject

An oil phantom and a human subject were used for imaging experiments. The phantom was made of glass capillaries (outer diameter = 5.0 mm and inner diameter = 4.2 mm) placed in an acrylic cylindrical container (outer diameter = 55 mm and inner diameter = 45 mm) filled with baby oil (Johnson & Johnson; Skillman, NJ, USA). The human subject was male (25-year-old) who was scanned repeatedly throughout this study.

Pulse Sequence for TB Measurements

A slice-selective 3D driven equilibrium spin-echo (3D-DESE) pulse sequence (Fig. 3) (13,20,21) was implemented in our system with the following parameters; repetition time (TR)/echo time (TE) = 80 ms/10 ms, slab thickness = 12 mm, image matrix size = 512 × 512 × 32, voxel size = 150 μm × 150 μm × 500 μm, and total imaging time = 23 min. The acquisition dwell time was 10 μs and pixel bandwidth 195 Hz. The excitation pulse was a 90 degree sinc ($\pm 4\pi$) pulse with 8 kHz bandwidth and 1 ms duration time. To minimize artifacts arising from imperfection of the 180° refocusing pulse, 180° phase-alternation of the refocusing pulse in successive phase-encoding steps was
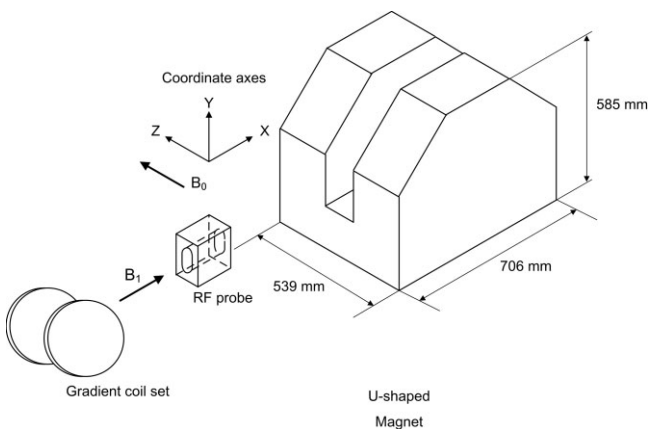
FIG. 2. The configuration of the permanent magnet, gradient coil set, and RF probe. The gradient coil set was fixed on the pole pieces of the magnet.
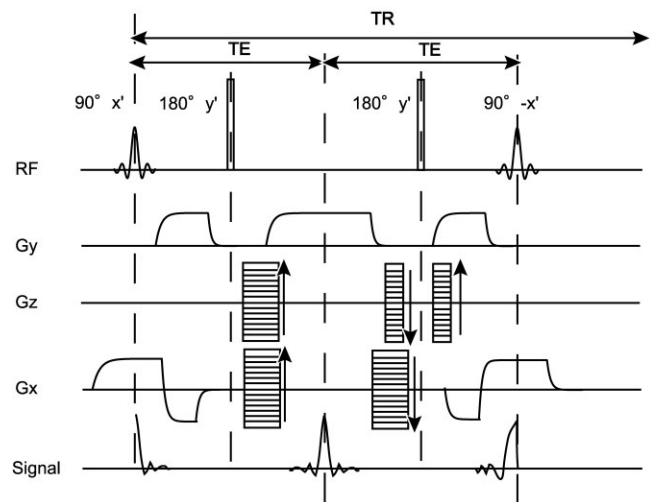
FIG. 3. Slice selective 3D-DESE sequence. The spin-echo time (10 ms) was minimized to optimize the SNR of the NMR signal.

applied. To reduce effects of gradient switching time (about 1 ms to 99% of the maximum value), which were caused by eddy currents on the RF shield box and time-dependent magnetic polarization of the magnetic material in the permanent magnet, the rewinding gradient was separated on both sides of the second 180° pulse. By using this technique, phase variation of the refocused echo throughout the *k*-space scan was reduced from about ±90° to about ±45°.

Experiments

The axes of the capillaries of the oil phantom were placed along the *x* direction (horizontal direction perpendicular to the *z* direction defined along the static magnetic field). The *y* direction was defined along the vertical direction perpendicular to the *z* direction. 3D MR images of the phantom were acquired with the 3D-DESE and a conventional 3D-SE sequence. The capillaries were used to evaluate geometrical distortions in the *yz* plane through the hexagonal array of the capillaries.

The image datasets were acquired using flexible image data-acquisition software (Sampler6; MRTechnology) with a time-sharing internal NMR lock mode (16). The NMR lock was applied just before the beginning of every 2D *k*-space data collection using the NMR signal of the whole object. With this technique, difference between the reference frequency and the Larmor frequency were kept at less than about 80 Hz throughout the image acquisition.

MR images of the subject were acquired after his left forearm was placed on the arm-holding table located in the magnet gap space and his wrist was inserted into the RF coil. The arm-holding table was made by horizontally stacking a 1-mm-thick copper plate and a 0.5-mm fiber-reinforced plastic plate onto a 45-mm-thick wooden block. The copper plate was connected to the RF shield of the probe to prevent external noise. The subject's forearm was connected to the ground by a capacitive coupling to the copper plate.

Before 3D image acquisition, a coronal scout view was acquired to determine the position of the distal radius. The total measurement time for the 3D image was about 23 min. For reproducibility evaluation, the left wrist of the same subject was scanned three times after repositioning.

RESULTS

Figure 4 shows axial 2D slices selected from 3D image datasets of the oil phantom acquired using 3D-DESE and 3D-SE sequences. Because Fig. 4b was acquired with the same pulse sequence as that used for the TB of the distal radius, it demonstrates possible image distortion and signal-to-noise ratio (SNR) observed in the TB volume.

Square shaped distortions observed for the outline of the acrylic container as shown in Fig. 4 were caused by nonlinearity of the magnetic field gradients. However, no apparent geometrical distortion was observed in the central region (about 30 mm diameter central circle) of the FOV. The phantom image acquired with the 3D-DESE sequence had an approximately 1.7 times SNR advantage compared with that acquired with the 3D-SE sequence.

Figure 5 shows a coronal scout view and cross-sectional images selected from a 1024 × 1024 × 64 voxel 3D image data set of the distal radius acquired with the 3D-DESE sequence. This dataset was obtained from doubly zero-filled Fourier interpolation of the original 512 × 512 × 32 voxel image. Thus, the voxel size was 75 μm × 75 μm × 250 μm. In Fig. 5b a solid circular region where geometric distortion is negligible is depicted as shown in Fig. 4b. SNR of the bone marrow signal was about 10 in Fig. 5b. This value is close to that obtained with a 1.5 T whole body MRI system (22–24).

Figure 6a shows a segmented image of the distal radius obtained from the original 512 × 512 × 32 voxel 3D image dataset. The segmentation was performed semi-automatically using a commercial software package (TRI3D/BON; Ratoc System Engineering, Tokyo, Japan). Figure 6b shows an image intensity histogram of the distal radius shown in Fig. 6a. This histogram is very similar to those reported for the distal radius using 1.5 T whole body MRI systems (9,10). This result suggests that our image data can be used for bone microstructure analysis, because the spatial resolution and SNR are sufficient for the previously reported analysis (25,26).
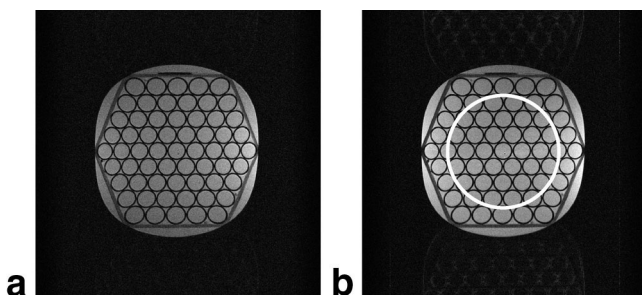
FIG. 5. **a:** Coronal scout view of the left wrist. The dark band shows the imaged slab. **b:** An axial cross-section selected from a 3D image dataset of the distal radius of the left wrist acquired with the 3D-DESE sequence. TR = 80 ms, TE = 10 ms, number of excitations (NEX) = 1, image matrix size = 512 × 512 × 32, voxel size = 150 μm × 150 μm × 500 μm. The diameter of the circle is 30 mm. **c:** Enlarged view of (b).

Figure 6d is a local histogram calculated for the cylindrical volume of interest (diameter = 6 mm and depth = 2 mm) as shown in Fig. 6c. This histogram shows a high intensity peak for bone marrow signal and low intensity broad distribution for voxels including bone and bone marrow.

Three image data sets of the wrist were analyzed using the digital topological analysis (DTA; MicroMRI Inc., Philadelphia, PA, USA) (12). The bone volume fraction (BVF) values calculated from three sets of the image data were 0.134, 0.144, and 0.139. As a result, the coefficient of variance (CV) of BVF was calculated to be 3.6%.

DISCUSSION

In this study we have developed a compact MRI system in which TB microstructure of the distal radius was clearly visualized in 23 min. Because the quality of our image is similar to those obtained with 1.5 T whole body MRI systems, our system could be used for clinical applications. However, some problems should be solved before clinical use.

The first problem is the measurement time. To reduce the measurement time, a higher SNR is highly desirable because TR can be reduced if the SNR is sufficient. The most straightforward solution to this problem is to use a smaller diameter RF coil. To make a smaller diameter RF coil for the distal radius, it should have an open-access structure. Another solution is to improve the pulse se-

FIG. 4. Cross-sectional images of the oil phantom acquired with (**a**) 3D-SE sequence and (**b**) 3D-DESE sequence. The diameter of the circle in (b) is 30 mm.
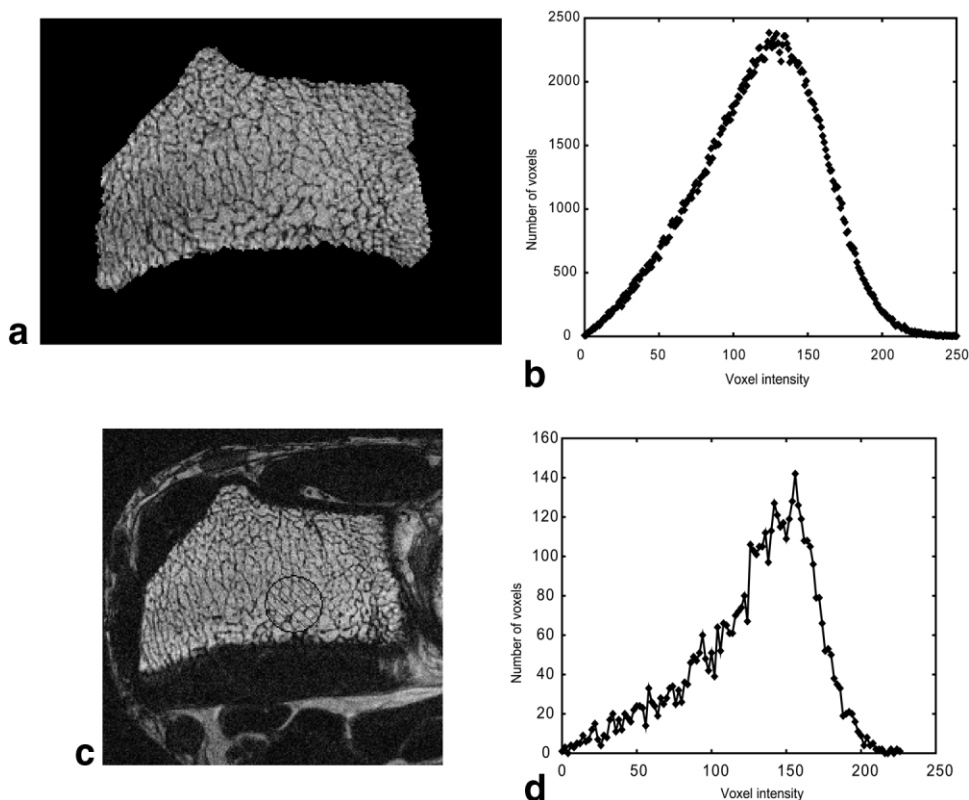
FIG. 6. **a:** Segmented image of the distal radius. **b:** Image intensity histogram obtained from 21 consecutive slices as shown in (a). **c:** Cylindrical volume of interest inside the distal radius. **d:** Image intensity histogram calculated for the cylindrical volume of interest in (c).

quence by using stronger magnetic field gradients to shorten the SE time. However, the eddy current and time dependent magnetic polarization of the magnetic materials should be precisely controlled to obtain good images. By combining these technical developments we believe an approximately 50% SNR improvement will be achieved to shorten the measurement time.

The second problem is the nonuniformity of the gradient fields. In longitudinal studies, where wrists of the subjects are scanned repeatedly at several months intervals, the reproducibility of bone parameters is essential. When the gradient field is not uniform, the bone parameters become sensitive to the position of the wrists in the FOV, even if the nonuniformity is corrected using image processing. Therefore, the gradient coil should be improved using some optimized design methods such as the target field method (27) or genetic algorithm (28).

The third problem is the immobilization of subjects and/or correction of the subject motion. Because our permanent magnet was originally designed for in vivo imaging of rats and mice, the subject was required to adopt an unnatural pose for the wrist imaging. The permanent magnet, gradient coil set, RF coil, and positioning system should be redesigned to allow natural positioning of subjects for clinical use. Nevertheless, we believe our results have demonstrated a feasibility of a permanent magnet compact MRI system as a clinical instrument for bone microstructure measurements of the distal radius.

CONCLUSION

We have developed a compact MRI system for TB microstructure measurements of the distal radius using a 1.0 T permanent magnet and a compact MRI console. TB microstructure of the distal radius was clearly visualized using a 3D-DESE sequence in a measurement time of 23 min. The image obtained had a sufficient quality for 3D bone microstructure analysis. We conclude that our system demonstrates the feasibility of a permanent magnet compact MRI as a clinical instrument for bone microstructure measurements of the distal radius.

REFERENCES

1. Kleerekoper M, Villanueva AR, Stanciu J, Sudhaker RD, Parfitt AM. The role of three-dimensional trabecular microstructure in the pathogenesis of vertebral compression fractures. Calcif Tissue Int 1985;37:594–597.
2. Recker RR. Architecture and vertebral fracture. Calcif Tissue Int 1993; 53(Suppl 1):S139–S142.
3. van Rietbergen B, Majumdar S, Newitt D, MacDonald B. High-resolution MRI and micro-FE for the evaluation of changes in bone mechanical properties during longitudinal clinical trials: application to calcaneal bone in postmenopausal women after one year of idoxifene treatment. Clin Biomech (Bristol, Avon) 2002;17:81–88.
4. Wehrli FW, Gomberg BR, Saha PK, Song HK, Hwang SN, Snyder PJ. Digital topological analysis of in vivo magnetic resonance microimages of trabecular bone reveals structural implications of osteoporosis. J Bone Miner Res 2001;16:1520–1531.

5. Benito M, Vasilic B, Wehrli FW, Bunker B, Wald M, Gomberg B, Wright AC, Zemel B, Cucchiara A, Snyder PJ. Effect of testosterone replacement on trabecular architecture in hypogonadal men. J Bone Miner Res, 2005;20:1785–1791.

6. Wehrli FW, Ladinsky GA, Vasilic B, Zemel BS, Wright AC, Song HK, Saha PK, Peachy H, Snyder PJ. Quantitative micro-MRI demonstrates significant effects on trabecular bone architecture in response to antiresorptive therapy. In: Proceedings of the 14th Annual Meeting of ISMRM, Seattle, WA, USA, 2006 (Abstract 546).

7. Majumdar S. Magnetic resonance imaging of trabecular bone structure. Top Magn Reson Imaging 2002;13:323–334.

8. Wehrli FW, Saha PK, Gomberg BR, Song HK, Snyder PJ, Benito M, Wright A, Weening R. Role of magnetic resonance for assessing structure and function of trabecular bone. Top Magn Reson Imaging 2002; 13:335–355.

9. Majumdar S, Genant HK, Grampp S, Newitt DC, Truong V-H, Lin JC, Mathur A. Correlation of trabecular bone structure with age, bone mineral density, and osteoporotic status: in vivo studies in the distal radius using high-resolution magnetic resonance imaging. J Bone Miner Res 1997;12:111–118.

10. Wehrli FW, Hwang SN, Ma J, Song HK, Ford JC, Haddad JG. Cancellous bone volume and structure in the forearm: noninvasive assessment with MR microimaging and image processing. Radiology 1998;206: 347–357.

11. Link TM, Majumdar S, Augat P, Lin JC, Newitt D, Lu Y, Lane NE, Genant HK. In vivo high resolution MRI of the calcaneus: differences in trabecular structure in osteoporosis patients. J Bone Miner Res 1998; 13:1175–1182.

12. Gomberg BR, Wehrli FW, Vasilic B, Weening RH, Saha PK, Song HK, Wright AC. Reproducibility and error sources of μ-MRI-based trabecular bone structural parameters of the distal radius and tibia. Bone 2004;35:266–276.

13. Iita N, Handa S, Tomiha S, Kose K. Development of a compact MRI for measurement of trabecular bone microstructure of the finger. Magn Reson Med 2007;57:272–277.

14. Boutroy S, Bouxsein ML, Munoz F, Delmas PD. In vivo assessment of trabecular bone microarchitecture by high-resolution peripheral quantitative computed tomography. J Clin Endocrinol Metab 2005;90:6508–6515.

15. Kose K, Haishi T, Adachi N, Uematsu T, Yoshioka H, Anno I. Development of an MR microscope using a portable MRI unit and a clinical whole body magnet. In: Proceedings of the 7th Annual Meeting of ISMRM, Philadelphia, PA, USA, 1999 (Abstract 2036).

16. Haishi T, Uematsu T, Matsuda Y, Kose K. Development of a 1.0 T MR microscope using a Nd-Fe-B permanent magnet. Magn Reson Imag 2001;19:875–880.

17. Kose K, Matsuda Y, Kurimoto T, Hashimoto S, Yamazaki Y, Haishi T, Utsuzawa S, Yoshioka H, Okada S, Aoki M, Tsuzaki T. Development of a compact MRI system for trabecular bone volume fraction measurements. Magn Reson Med 2004;52:440–444.

18. Miyamoto T, Sakurai H, Takahashi H, Aoki M. A development of a permanent magnet assembly for MRI devices using Nd-Fe-B material. IEEE Trans Magn 1989;25:3907–3909.

19. Sagawa M, Fujimura S, Togawa H, Yamamoto H, Matsuura Y. New material for permanent magnets on a base of Nd and Fe. J Appl Phys 1984;55:2083–2087.

20. Iwaoka H, Sugiyama T, Matsuura H, Fujino K. A new pulse sequence for "fast recovery" fast-scan NMR imaging. IEEE Trans Med Imaging 1984;3:41–46.

21. Hargreaves BA, Gold GE, Lang PK, Conolly SM, Pauly JM, Bergman G, Vandevenne J, Nishimura DG. MR imaging of articular cartilage using driven equilibrium. Magn Reson Med 1999;42:695–703.

22. Ma J, Wehrli FW, Song HK. Fast 3D large-angle spin-echo imaging (3D FLASE). Magn Reson Med 1996;35:903–910.

23. Techawiboonwong A, Song HK, Magland JF, Saha PK, Wehrli FW. Implication of pulse sequence in structural imaging of trabecular bone. J Magn Reson Imag 2005;22:647–655.

24. Magland J, Vasilic B, Wehrli FW. Fast low-angle dual spin-echo (FLADE): a new robust pulse sequence for structural imaging of trabecular bone. Magn Reson Med 2006;55:465–471.

25. Hwang SH, Wehrli FW. Estimating voxel volume fractions of trabecular bone on the basis of magnetic resonance images acquired in vivo. Int J Imag Syst Tech 1999;10:186–198.

26. Hwang SH, Wehrli FW. Subvoxel processing: a method for reducing partial volume blurring with application to in vivo MR images of trabecular bone. Magn Reson Med 2000;47:948–957.

27. Turner R. A target field approach to optimal coil design. J Phys D (Appl Phys) 1986;19:147–151.

28. Goldberg DE. Genetic algorithms in search, optimization and machine learning, 1st ed. Addison-Wesley Longman Publishing Co., Inc. Boston: MA, 1989.